

Ka-Band Atmospheric Noise-Temperature Measurements at Goldstone, California, Using a 34-Meter Beam-Waveguide Antenna

D. Morabito,¹ R. Clauss,² and M. Speranza³

System operating noise temperature, T_{op} , data acquired during the Summer Undergraduate Research Fellowship Satellite (SURFSAT-1) link experiment at the 34-meter research and development antenna, DSS 13, at Goldstone, California, were used to estimate the noise contribution due to the atmosphere at both Ka-band (32 GHz) and X-band (8.4 GHz). Data from 192 tracking passes conducted between November 1995 and October 1996 were acquired over a wide range of elevation angles (or air masses).

The T_{op} data were recorded as the antenna tracked the spacecraft in elevation angle (antenna “tipping” curves). These data were least-squares fitted to estimate the equivalent atmospheric noise contribution and attenuation of one mass of atmosphere (at antenna zenith or a 90-deg elevation angle) at Ka-band. The statistics and cumulative distributions of these measurements will be presented along with intercomparisons of independent estimates derived from concurrent water vapor radiometer data and a model using input surface meteorological data.

I. Introduction

The NASA Deep Space Network (DSN) is evaluating the use of the Ka-band (32-GHz) downlink frequency band for deep-space telecommunications. Ka-band (32 GHz) is 3.8 times higher in frequency than the DSN’s operational X-band (8.4-GHz) frequency. Ka-band provides an advantage of 11.6 dB (a ratio of 14.5 or 3.8^2) over X-band in the spacecraft effective isotropic radiated power (EIRP) when the same spacecraft transmitter output power and the same effective antenna size are used. In practice, the Ka-band downlink advantage over X-band is reduced to about 7 dB due to higher atmospheric noise, decreased ground station antenna efficiency, and increased weather susceptibility. This higher Ka-band advantage, relative to X-band, can be used to reduce cost, power, mass, or volume of future deep-space radio telecommunications systems on board spacecraft or to allow for higher data rates. It is important

¹ Communications Systems and Research Section.

² Spacecraft Telecommunications Equipment Section.

³ Student at Rensselaer Polytechnic Institute, Troy, New York.

to statistically characterize Ka-band atmospheric effects at the specific DSN tracking sites in order to quantify the advantages of using Ka-band.

The Summer Undergraduate Research Fellowship Satellite (SURFSAT-1) link experiment provided spacecraft signal strength measurements at both Ka-band and X-band using the NASA DSN research and development (R&D) 34-meter beam-waveguide antenna, DSS 13, at Goldstone, California. In addition to signal strength, total power radiometer (TPR) data were acquired for the purpose of noise calibration. X-band and Ka-band TPR data from 192 of these experiments, conducted between November 1995 and October 1996, were acquired over a wide range of elevation angles (or air masses).

The TPR system operating noise temperature, T_{op} , data were recorded as the antenna tracked the spacecraft in elevation angle (antenna “tipping” curves). The antenna’s field of view (beam) over a track encountered one air mass at zenith to 5.5 air masses at a 10.5-deg antenna elevation angle. These T_{op} -versus-elevation-angle tip-curve data were least-squares fitted to estimate the equivalent atmospheric noise contribution, T_{atm} , and attenuation of one mass of atmosphere (antenna zenith or a 90-deg elevation angle) at Ka-band. The statistics and cumulative distributions of these measurements will be presented along with intercomparisons of independent estimates derived from concurrent water vapor radiometer (WVR) data and a model using input surface meteorological data.

II. System Description and Data Acquisition

The SURFSAT-1 tracking data were acquired at DSS 13, a 34-meter beam-waveguide (BWG) antenna (Fig. 1) located at the Goldstone Deep Space Communications Complex near Barstow, California, in the Mojave Desert. The passes occurred within 3 hours of sunrise and sunset and typically were 5 to 20 minutes in duration. A total of 418 tracking passes were conducted between launch (November 1995) and December 1996. The elevation angles of the observations ranged from 7 deg to as high as 90 deg,



Fig. 1. The DSS-13 34-m research and development BWG antenna at Goldstone, California.

depending upon the particular track across the sky. The X-/Ka-band data acquisition ended on December 31, 1996, when a command was uplinked to switch SURFSAT-1's signal from the X-/Ka-band transponder and beacons to the 14–15 GHz (Ku-band) transponder for the purpose of testing the operational space very long baseline interferometry (SVLBI) ground stations at Ku-band.

The BWG antenna, depicted schematically in Fig. 2, consists of a main reflector that focuses the incident received energy onto a subreflector, which then channels the energy via a series of mirrors (inside the beam-waveguide tubes) down into a subterranean pedestal room. There a central ellipsoid mirror channels the energy to one of several feed stations arranged about a concentric ring on the pedestal room floor. The X-/Ka-band feed package system includes an X-/Ka-band dichroic mirror that reflects the longer-wavelength X-band energy into the X-band feedhorn. The dichroic plate passes the shorter-wavelength Ka-band energy to an ellipsoid mirror on the ceiling, which then reflects it down into the Ka-band feedhorn.

The signals incident to the feedhorns are amplified by cryogenically cooled high-electron mobility transistor (HEMT) low-noise amplifiers (LNAs) and downconverted to 300-MHz intermediate-frequency (IF) signals that are sent to a control room via fiber-optic cables. In the control room, an experimental tone tracker (ETT) and Hewlett-Packard spectrum analyzers record the signals, which include signal strengths for the link experiment. The received signal data in the form of signal-to-noise ratios (SNRs) in dB-Hz are later converted to received signal strengths using the TPR data for noise calibration.

The X-/Ka-band link experiment was conducted for the purpose of evaluating the advantage of Ka-band relative to X-band by simultaneously tracking both X-band and Ka-band signals emitted by the spacecraft. As the angle between the boresight of each spacecraft antenna changes relative to the direction of the receiving station, the signature in the received signal level changes. These signatures are modeled using the ground station gain, an atmospheric attenuation model, the range to the spacecraft

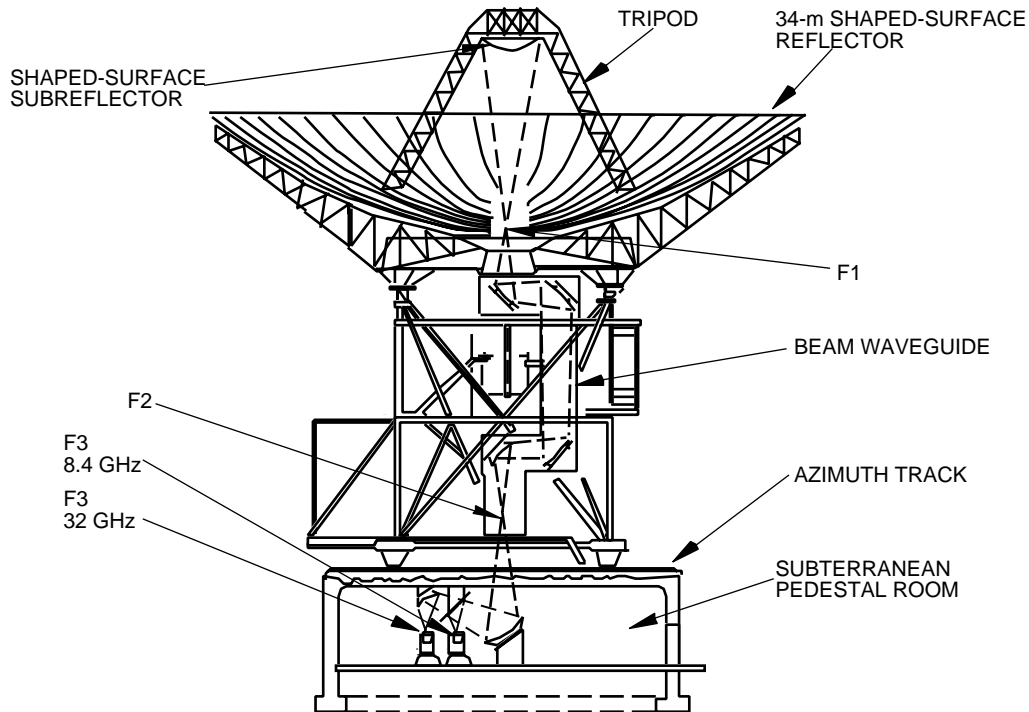


Fig. 2. Geometric configuration of reflectors and mirrors of the DSS-13 BWG antenna along with the positions of the focal points (F1, F2, and F3).

for space loss, and the preflight spacecraft antenna patterns. This assumes that the orientation of the satellite remains stable in a known coordinate system as it orbits the Earth. However, shortly after launch, it became apparent that the spacecraft was not in its intended gravity gradient-stabilized, nadir-pointed orientation. Furthermore, it also became apparent that the satellite was experiencing dynamic motion, which has not yet been modeled. The link experiment work was deferred due to this unanticipated dynamic motion. However, the TPR data acquired during these SURFSAT-1 tracks were used to estimate atmospheric noise temperatures that are useful for statistical characterization of the atmosphere at Ka-band at the Goldstone tracking site and for intercomparisons with similar estimates using other methods.

The TPR measures total noise power in each channel after bandpass filtering (20 MHz for 8.4 GHz and 30 MHz for 32 GHz) to limit the noise coming in so that radio frequency interference (RFI) can be minimized. The bandwidth of these filters together with the radiometer integration time (usually 5 s) define the contribution of the random fluctuations of the temperature measurements that lies below 0.01 K. Measurements of the total IF noise power are made using power sensors followed by power meters—one set each for 8.4 GHz and 32.0 GHz. The power sensors measure between 100-picowatt and 10- μ watt input power levels.

Calibrations were performed prior to the start of each session of two to three successive tracks. During each calibration, the TPR measured the total IF noise power while the input to the HEMT was switched from (1) sky to (2) sky-plus-noise diode to (3) ambient load to (4) ambient load-plus-noise diode. Transfer functions, derived from these calibrations [1], were used to convert the received power levels to estimates of calibrated system operating noise temperature, T_{op} , during the track. These calibrations also allowed for the estimation of any nonlinearity that may have been present in the system.

The T_{op} measurements from the TPR were considered the raw data. The spacecraft signals were outside the TPR filter bandwidths; thus the T_{op} -versus-elevation angle signature depended only on the ground antenna and atmosphere noise-temperature elevation-angle dependence as the satellite was tracked. Of the 418 SURFSAT-1 passes conducted, the TPR data from 192 of these passes were deemed usable for this study. Passes not included in the study included 155 passes that employed other Ka-band feed packages (array feed and monopulse). As these other feed packages were used for special experimental and testing activities, these systems were not fully characterized for inclusion in this study. The remaining 71 passes were not included in the study due to the following: 7 passes with insufficient arc in elevation angle, 12 passes involving equipment failure, 38 passes involving data file problems, 13 passes conducted at X-band only, and 1 pass conducted while the station was transmitting.

WVR data [2] were acquired concurrently during the tracks for intercomparison with the TPR results. One set of WVR data was obtained from the R6 WVR (April 1996 to December 1996), and the other set acquired from the J3 WVR (November 1995 to March 1996). The R6 WVR is a small stand-alone package positioned near the BWG antenna that determines the presence of water in the atmosphere in vapor and droplet form along the WVR beam by measuring noise levels at 20.7 and 31.4 GHz over RF bandwidths of 200 MHz. It consists of a platform with a small feedhorn and mirror assembly that can observe any point in the sky. It is located 300 m from the BWG antenna on the roof of the control building. The R6 WVR has been operating nearly continuously at DSS 13 since October 1993 in a tipping-curve mode. This instrument operates in all non-rain conditions and performs periodic tip curves from zenith to elevations of 42 and 30 deg, at azimuths of 35 and 195 deg. Each tip curve requires about 4.25 minutes. The WVR produces sky brightness temperatures at frequencies of 20.7 and 31.4 GHz. The WVR IF bandwidth is 100 MHz (double-sideband), and its beamwidth is about 7 deg with a positional accuracy of 0.5 deg. The measurement precision of the WVRs is about 0.1 K, and the absolute uncertainty is about 0.5 K, based on intercomparisons with other radiometers.

The J3 WVR is a three-channel Dicke radiometer operating at frequencies of 20.7, 22.2, and 31.4 GHz. It is fed by a single horn positioned on a horizontal axis that views a 45-deg reflector through a circular Teflon reflective window. The reflector rotates about the horn axis to produce scans in elevation. Azimuth

position is achieved by rotation of the radiometer enclosure. Noise diode sources, after calibration via tip curves, are used to monitor gain fluctuations. The scalar feed horn produces half-power beam widths of approximately 9, 8, and 6 deg for the 20.7-, 22.2-, and 31.4-GHz channels, respectively. The J3 WVR is located on a concrete pad approximately 50 m from the BWG antenna and has been operating primarily in a tip-curve mode since its deployment in January 1995. Each tip curve requires approximately 2 minutes and produces three-channel sky brightness temperatures at zenith and the 30- and 42-deg elevation positions that are comparable in accuracy and precision to the R6 WVR measurements.

The measured sky-brightness temperature from the WVRs at 31.4 GHz was converted to an equivalent one-air-mass atmospheric noise temperature for the purpose of intercomparison with the estimates from the BWG TPR data. The effective cosmic background temperature was removed from the raw 31.4-GHz WVR data, and a small correction was applied to refer the measurements to 32.0 GHz. For the X-band intercomparison, the WVR Ka-band estimate was converted to the X-band frequency by using a conversion formula derived from Desert Rock, Nevada, radiosonde data.⁴

Magnitudes and deviations of one-air-mass T_{atm} measured by the two systems are cross-compared in the study. One expects good agreement between the BWG and WVR measurements on dry clear days when the water vapor content is minimal, and larger differences between the measurements during cloudy conditions. The results of the cross-comparison are presented in Section IV.

The weather system samples and records a range of meteorological parameters, including atmospheric pressure, air temperature, relative humidity, wind speed, and wind direction. The data are stored locally and routed through the station’s monitor and control computer to a central storage device. The surface measurements are input to a surface model [3], producing T_{atm} estimates that then can be compared with those measured from the BWG tipping curves and the WVR.

III. Model and Fit Strategy

The model and fit strategy closely follows that of a previous study on an earlier set of tip-curve data acquired during the Ka-band Antenna Performance (KaAP) experiments [4]. The T_{op} measurements output from the TPR are considered the raw data. These data are converted to prefit residuals by removing the nonatmosphere-dependent contributions, which include the ground temperature contribution due to tripod scatter and spillover, $T_{ant}(\theta)$ versus elevation angle θ , and equipment contributions, $T_{equipment}$, due to the LNA and follow-on equipment:

$$T_{observed}(\theta) = T_{op}(\theta) - T_{ant}(\theta) - T_{equipment} \quad (1)$$

The remaining signature in $T_{observed}(\theta)$, assumed to be atmosphere dependent, is modeled using a two-layer atmospheric model from Kutner [5]. This model takes advantage of the fact that the oxygen, O_2 , is well distributed in the atmosphere with a pressure scale height of about 8 km while the water vapor, H_2O , is concentrated in the lower 2 km near the ground. These two contributions can be treated separately, which is important since the O_2 is relatively constant in time while the H_2O can change significantly over short time scales. The prefit residuals in Eq. (1), $T_{observed}(\theta)$, are fit using the following model:

$$T_{model}(\theta) = B + \frac{T_{cb}/L_{atm}(\theta) + T_{atm}(\theta)}{L_{ant}} \quad (2)$$

where

⁴S. Keihm, “Conversion of WVR 31.4 GHz Zenith TB Measurements to X-Band,” JPL Interoffice Memorandum 3833-94-440/SJK (internal document), Jet Propulsion Laboratory, Pasadena, California, December 15, 1994.

- B = a bias term, K
- T_{cb} = the effective cosmic background from Planck’s law (2.5 K at X-band; 2.0 K at Ka-band)
- $L_{atm}(\theta)$ = total atmospheric attenuation ($e^{[\tau_{O_2} + \tau_{H_2O}]A(\theta)}$)
- L_{ant} = the antenna loss factor
- θ = the antenna elevation angle

and the atmosphere contribution in Eq. (2) is given by Kutner’s two-layer model [5]:

$$T_{atm}(\theta) = T_{O_2} \left[1 - e^{-\tau_{O_2}A(\theta)} \right] e^{-\tau_{H_2O}A(\theta)} + T_{H_2O} \left[1 - e^{-\tau_{H_2O}A(\theta)} \right] \quad (3)$$

where

- T_{O_2} = the physical temperature of oxygen (260 K)
- τ_{O_2} = the opacity of the oxygen contribution
- $A(\theta)$ = the air-mass number ($\sim 1/\sin \theta$)
- τ_{H_2O} = the opacity of the water vapor contribution
- T_{H_2O} = the physical temperature of the water vapor ($T_{surface} - 10$ K)
- $T_{surface}$ = the air temperature (K) obtained from the surface meteorological data

The following residual model is constructed using the prefit data of Eq. (1) and the model of Eq. (2) with a priori values derived from the surface model:

$$\Delta T_{residual}(\theta) = T_{observed}(\theta) - T_{model}(\theta) \quad (4)$$

The Ka-band residual data in Eq. (4) at elevation angles, θ , above 10.5 deg (5.5 air masses) were iteratively least-squares fit, producing estimates of the bias term, B , and the opacity of the water vapor contribution, τ_{H_2O} , for each pass. The bias term, B , accounts for any unmodeled bias. The range of elevation angles over which a fit was actually made depends upon the particular satellite track in the sky. The opacity of oxygen, τ_{O_2} , used in the model was estimated from an atmospheric noise temperature emission model [3] using surface weather data as input.

The postfit residuals after convergence are computed using Eq. (4) with values of B and τ_{H_2O} output from the least-squares fit. The scatter in these residuals is a measure of the “goodness” of the fit and/or the “bumpiness” of the atmosphere variations over the pass. Estimates of the equivalent one-air-mass atmospheric noise temperature, T_{atm} , are then computed using Eq. (3) with $\theta = 90$ deg and τ_{H_2O} from the solution.

For this study, the concurrent X-band data acquired during the pass were not least-squares fit. Instead, the X-band postfit residuals presented are the difference between the X-band prefit residuals, Eq. (1), and the equivalent X-band model, Eqs. (2) and (3), using the water vapor opacity, τ_{H_2O} , fit from the Ka-band data, scaled appropriately to X-band. Any systematic trends in the resulting X-band postfit residuals provide an indication of how the X-band model behaves over a pass. As functions of elevation angle that repeat for a set of clear weather passes, these trends, or signatures, can be assumed to be due to any unmodeled X-band antenna-temperature elevation dependence. It is intended that these X-band residuals will be used as a focus of a future study to improve the X-band antenna model, $T_{ant}(\theta)$.

IV. Results

Table 1 summarizes the results of the data analysis for each pass.

Examples of raw T_{op} data and postfit residuals are presented here for two cases: a clear-weather pass (Fig. 3) and a cloudy-/rainy-weather pass (Fig. 4). Figures 3(a) and 3(b) display the raw X-band and Ka-band T_{op} data, respectively, for the case of a clear-weather pass. Figures 3(c) and 3(d) display the resulting postfit X-band and Ka-band residuals, respectively. The low 0.18-K rms scatter of the Ka-band postfit residuals of Fig. 3(d) is consistent with the noise in the data being limited by gain instability (0.2 percent). Figures 4(a) through 4(d) display the corresponding plots for the case of a rainy-weather pass, where the higher rms scatter is a measure of the turbulence in the weather. By inspecting the postfit residuals, one sees a significant variation of the atmospheric noise over the pass about a mean-fitted value. A focus of a proposed future study is to partition a single pass into segments (in steps of one air mass or less) and solve for the zenith T_{atm} along the line of sight as a function of time.

The BWG T_{op} measurement error sources are dominated by gain instability, which is about 0.2 K over the typical 10-minute measurement period, and atmospheric fluctuations. The atmosphere-induced fluctuations usually are comparable or even below the gain instability contribution during clear-weather

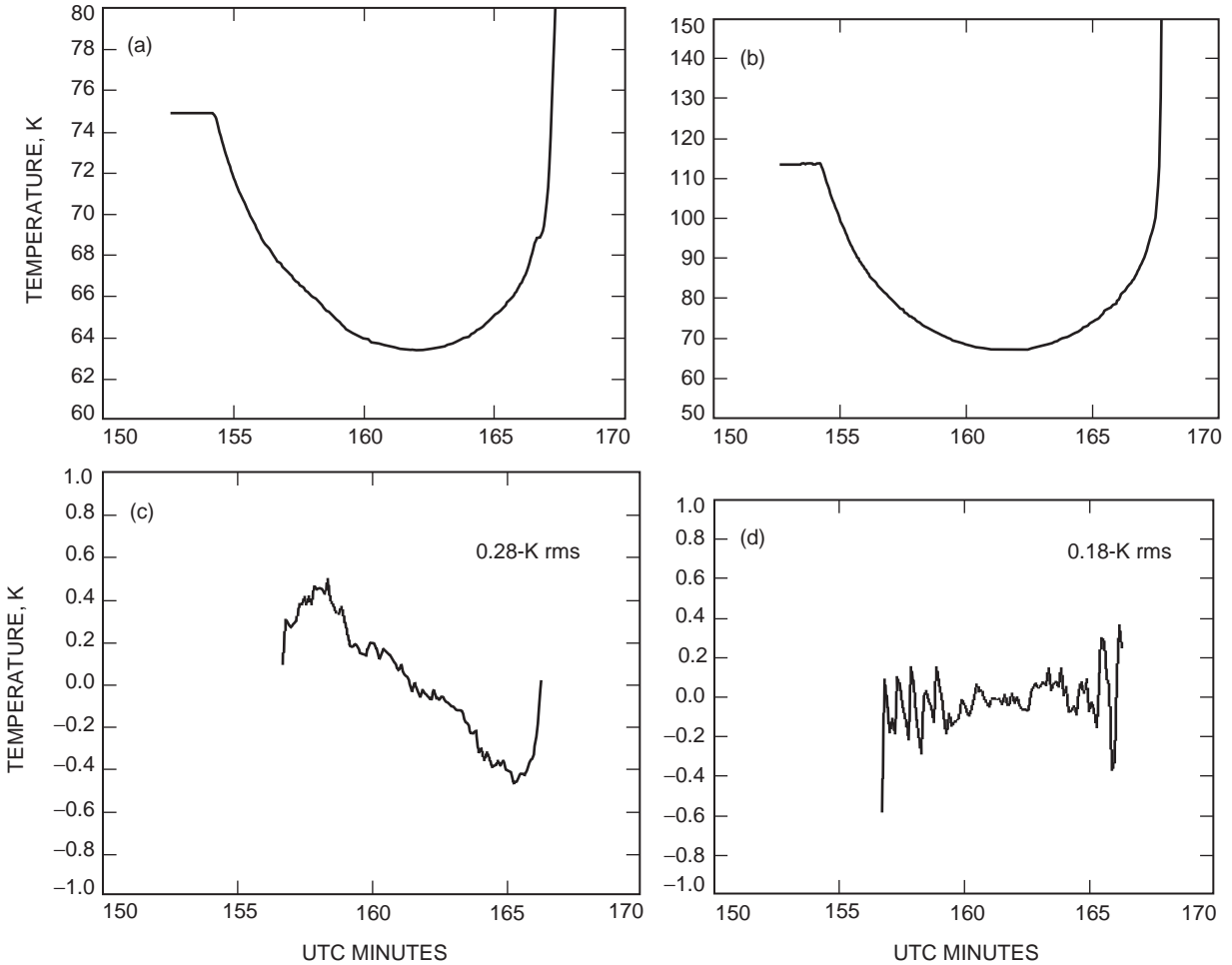


Fig. 3. Examples of clear-weather data acquired during pass 96-150b: (a) raw X-band T_{op} data, (b) raw Ka-band T_{op} data, (c) X-band postfit residuals using the model derived from the Ka-band postfit solution, and (d) Ka-band postfit residuals corresponding to the fit of data from Fig. 3(b).

Table 1 (cont'd).

(1) Experiment ID, yr-doyx ^a	(2) Min. elev. angle over fit TPR data, deg	(3) Max. elev. angle over fit TPR data, deg	(4) X-band T_{atm} at zenith, ^b K	(5) X-band T_{atm} at zenith, ^c K	(6) Est. $\frac{3}{4}$ of (5), K	(7) X-band T_{atm} at zenith, ^d K	(8) Est. $\frac{3}{4}$ of (7), K	(9) Difference of (5) and (7), ^e K	(10) Ka-band T_{atm} at zenith, ^b K	(11) Ka-band T_{atm} at zenith, ^c K	(12) Est. $\frac{3}{4}$ of (11), K	(13) Ka-band T_{atm} at zenith, ^f K	(14) Est. $\frac{3}{4}$ of (13), K	(15) Difference of (11) and (13) ^e
95-333b	10.3	21.5	2.30	2.51	0.27	—	—	—	8.43	10.96	0.71	—	—	—
95-333d	10.1	10.5	2.34	—	—	—	—	—	8.94	11.77	0.04	—	—	—
95-334a	14.5	64.2	2.28	2.41	0.49	—	—	—	8.30	9.82	0.61	—	—	—
95-334b	13.5	89.8	2.28	2.36	0.29	—	—	—	8.25	9.29	0.87	—	—	—
95-334c	10.3	83.7	2.32	2.39	0.12	—	—	—	8.70	9.50	0.53	—	—	—
95-334d	10.1	13.5	2.31	2.38	0.16	—	—	—	8.75	9.62	0.10	—	—	—
95-335a	10.2	53.5	2.27	2.29	0.48	—	—	—	8.28	8.49	0.73	—	—	—
95-335b	10.2	32.1	2.26	2.29	0.32	—	—	—	8.01	8.40	0.43	—	—	—
95-340a	10.2	82.0	2.39	2.52	0.83	—	—	—	9.75	11.36	1.03	—	—	—
95-340b	10.1	13.7	2.48	2.58	0.30	—	—	—	11.00	12.08	0.59	—	—	—
95-341a	10.3	85.4	2.44	2.56	0.70	—	—	—	10.48	11.82	0.74	—	—	—
95-341b	14.1	17.7	2.46	2.53	0.14	—	—	—	10.67	11.41	0.40	—	—	—
95-341c	10.5	68.5	2.51	2.62	0.12	—	—	—	11.30	12.59	0.50	—	—	—
95-342a	10.5	70.9	2.33	2.38	0.59	—	—	—	9.15	9.69	1.16	—	—	—
95-342b	10.2	22.1	2.35	2.42	0.33	—	—	—	9.40	10.14	0.69	—	—	—
96-008a	10.2	15.8	2.26	2.32	0.40	—	—	—	8.19	8.92	0.89	—	—	—
96-009a	10.3	73.4	2.28	2.36	0.70	—	—	—	8.28	9.26	1.00	—	—	—
96-010a	10.2	88.0	2.28	2.43	0.92	—	—	—	8.40	10.17	0.78	—	—	—
96-010b	10.1	10.6	2.31	2.66	0.28	—	—	—	8.74	12.90	1.45	—	—	—
96-011b	10.2	14.4	2.27	2.26	0.25	—	—	—	8.06	7.81	0.45	—	—	—
96-016a	10.2	49.4	2.38	2.41	0.70	—	—	—	9.78	10.15	0.88	—	—	—
96-016c	10.2	37.9	2.46	2.65	0.21	—	—	—	10.64	12.93	0.59	—	—	—
96-017a	10.4	25.9	2.33	2.27	0.19	—	—	—	9.29	8.41	0.51	—	—	—
96-017b	10.3	47.5	2.32	2.30	0.28	—	—	—	9.01	8.81	0.30	—	—	—

^a Where yr is the year, doy is the day of the year, and x is the pass designator (a, b, c, etc.).

^b Determined from surface meteorological data.

^c Determined from fit to TPR data.

^d Determined from linear fit to WVR 31.4 GHz during the period of fit of BWG TPR data and corrected to X-band.

^e T_{atm} (BWG) $_i$ T_{atm} (WVR).

^f Determined from linear fit to WVR 31.4 GHz during the period of fit of BWG TPR data.

Table 1 (cont'd).

(1) Experiment ID, yr-doyx ^a	(2) Min. elev. angle over fit TPR data, deg	(3) Max. elev. angle over fit TPR data, deg	(4) X-band T_{atm} at zenith, ^b K	(5) X-band T_{atm} at zenith, ^c K	(6) Est. $\frac{3}{4}$ of (5), K	(7) X-band T_{atm} at zenith, ^d K	(8) Est. $\frac{3}{4}$ of (7), K	(9) Difference of (5) and (7), ^e K	(10) Ka-band T_{atm} at zenith, ^b K	(11) Ka-band T_{atm} at zenith, ^c K	(12) Est. $\frac{3}{4}$ of (11), K	(13) Ka-band T_{atm} at zenith, ^f K	(14) Est. $\frac{3}{4}$ of (13), K	(15) Difference of (11) and (13) ^e
96-018a	10.2	80.4	2.29	2.36	0.75	—	—	—	8.55	9.33	1.06	—	—	—
96-023a	10.3	30.3	2.20	2.36	0.11	—	—	—	7.33	9.19	0.22	—	—	—
96-023b	10.4	32.5	2.24	2.28	0.40	—	—	—	7.71	8.07	0.73	—	—	—
96-024a	10.1	23.9	2.20	2.35	0.57	—	—	—	7.07	8.94	0.85	—	—	—
96-024b	10.4	41.7	2.20	2.55	0.67	—	—	—	6.99	11.24	0.91	—	—	—
96-025a	10.4	53.9	2.29	2.29	0.70	—	—	—	8.42	8.45	0.93	—	—	—
96-025b	10.1	14.5	2.31	2.24	0.42	—	—	—	9.04	8.23	0.41	—	—	—
96-026a	10.4	69.7	2.33	2.27	0.89	—	—	—	9.13	8.36	1.51	—	—	—
96-030a	10.4	43.6	2.27	2.40	0.72	2.42	0.02	i 0.02	8.36	9.99	0.84	10.51	0.10	i 0.52
96-030b	10.1	21.3	2.25	2.44	0.34	2.41	0.03	0.03	8.03	10.33	0.64	10.19	0.12	0.14
96-037a	10.5	86.5	2.70	2.94	0.47	2.59	0.02	0.35	13.37	16.19	2.16	14.01	0.13	2.18
96-037b	10.1	13.6	2.69	2.69	0.34	2.58	0.02	0.11	13.21	13.11	0.78	13.85	0.11	i 0.74
96-037c	10.2	15.9	2.66	2.57	0.14	2.50	0.02	0.07	12.74	11.52	0.34	12.17	0.12	i 0.65
96-037d	10.1	89.0	2.67	2.57	0.34	2.50	0.03	0.08	12.78	11.61	0.98	12.16	0.15	i 0.56
96-038a	10.2	50.2	2.56	2.46	0.58	2.46	0.04	0.00	11.73	10.50	1.12	11.32	0.16	i 0.82
96-038b	10.1	85.4	2.53	2.52	0.32	2.44	0.02	0.08	11.34	11.17	1.00	10.87	0.11	0.29
96-038d	10.2	78.1	2.39	2.36	0.19	2.37	0.03	i 0.01	9.75	9.29	0.33	9.33	0.14	i 0.04
96-039b	10.3	65.0	2.27	2.32	0.13	2.35	0.02	0.03	8.35	8.93	0.32	8.97	0.09	i 0.04
96-039c	10.3	25.4	2.28	—	—	2.33	0.03	—	8.44	9.22	0.26	8.50	0.10	0.73
96-040a	10.4	31.0	2.26	2.31	0.60	2.35	0.05	i 0.04	8.48	8.98	0.95	8.89	0.20	0.09
96-040b	10.3	31.0	2.27	2.27	0.38	2.36	0.03	i 0.09	8.50	8.44	0.69	9.12	0.10	i 0.68
96-040c	10.4	53.7	2.24	2.35	0.13	2.38	0.03	i 0.03	8.05	9.40	0.58	9.68	0.12	i 0.28
96-045a	10.5	74.6	2.47	2.64	0.65	2.54	0.03	0.10	10.71	12.71	1.29	12.98	0.17	i 0.27
96-045c	10.1	19.6	2.43	2.48	0.15	2.42	0.03	0.06	10.08	10.67	1.88	10.53	0.13	0.14

^a Where yr is the year, doy is the day of the year, and x is the pass designator (a, b, c, etc.).

^b Determined from surface meteorological data.

^c Determined from fit to TPR data.

^d Determined from linear fit to WVR 31.4 GHz during the period of fit of BWG TPR data and corrected to X-band.

^e T_{atm} (BWG) i T_{atm} (WVR).

^f Determined from linear fit to WVR 31.4 GHz during the period of fit of BWG TPR data.

Table 1 (cont'd).

(1) Experiment ID, yr-doyx ^a	(2) Min. elev. angle over fit TPR data, deg	(3) Max. elev. angle over fit TPR data, deg	(4) X-band T_{atm} at zenith, ^b K	(5) X-band T_{atm} at zenith, ^c K	(6) Est. $\frac{3}{4}$ of (5), K	(7) X-band T_{atm} at zenith, ^d K	(8) Est. $\frac{3}{4}$ of (7), K	(9) Difference of (5) and (7), ^e K	(10) Ka-band T_{atm} at zenith, ^b K	(11) Ka-band T_{atm} at zenith, ^c K	(12) Est. $\frac{3}{4}$ of (11), K	(13) Ka-band T_{atm} at zenith, ^f K	(14) Est. $\frac{3}{4}$ of (13), K	(15) Difference of (11) and (13) ^e
96-045d	10.1	79.3	2.41	2.37	0.12	2.40	0.03	i 0.03	9.91	9.32	1.24	9.95	0.12	i 0.64
96-045e	10.2	15.7	2.38	2.59	0.35	2.38	0.01	0.21	9.65	12.16	1.43	9.64	0.05	2.52
96-046c	10.2	19.5	2.33	2.46	0.52	2.37	0.02	0.10	9.00	10.58	0.32	9.32	0.09	1.27
96-051a	10.1	59.7	2.62	2.85	0.61	2.71	0.03	0.14	12.81	15.56	0.78	16.11	0.21	i 0.55
96-053b	10.2	23.3	2.31	2.30	0.13	2.33	0.05	i 0.03	8.64	8.44	0.35	8.43	0.17	0.01
96-058a	16.4	86.7	2.17	—	—	—	—	—	7.06	12.75	1.34	—	—	—
96-058b	10.4	41.6	2.17	2.26	0.67	2.32	0.04	i 0.06	6.86	7.96	1.07	8.08	0.13	i 0.12
96-059a	10.2	18.7	2.31	2.32	0.66	2.44	0.26	i 0.12	8.58	8.71	4.17	10.92	1.17	i 2.21
96-060a	10.2	67.8	—	2.33	0.76	2.37	0.03	i 0.04	—	8.82	1.18	9.39	0.11	i 0.57
96-065a	10.2	41.2	2.64	2.58	0.63	2.49	0.02	0.09	12.98	12.18	0.94	12.06	0.08	0.11
96-065b	10.4	46.5	2.62	2.68	0.39	2.52	0.05	0.17	12.70	13.42	1.05	12.59	0.23	0.83
96-066a	10.3	54.1	2.18	2.25	0.19	2.32	0.04	i 0.07	6.86	7.61	0.54	8.13	0.12	i 0.52
96-066b	10.4	34.6	2.18	2.29	0.22	2.32	0.04	i 0.03	6.73	8.13	0.35	8.20	0.15	i 0.07
96-067a	10.2	25.4	2.15	2.21	0.10	—	—	—	6.62	7.29	0.18	—	—	—
96-067b	14.0	48.2	2.17	2.22	0.12	—	—	—	6.75	7.38	0.24	—	—	—
96-072a	10.7	59.3	2.34	2.41	0.63	—	—	—	9.32	10.10	1.14	—	—	—
96-072b	10.4	21.9	2.39	—	—	—	—	—	9.82	10.36	0.55	—	—	—
96-073a	10.1	48.5	2.55	2.71	1.11	—	—	—	11.93	13.75	8.82	—	—	—
96-073b	10.4	27.9	2.45	2.39	0.27	—	—	—	10.64	9.86	0.29	—	—	—
96-073c	10.3	72.2	2.45	3.69	1.83	—	—	—	10.60	25.34	13.47	—	—	—
96-073d	10.4	26.0	2.45	6.53	3.30	—	—	—	10.66	56.19	16.06	—	—	—
96-078a	10.2	27.5	2.24	2.34	0.17	2.38	0.05	i 0.04	7.99	9.21	0.48	9.64	0.18	i 0.43
96-078b	10.1	61.9	2.25	2.41	0.14	2.39	0.03	0.01	8.10	9.96	0.24	9.92	0.12	0.04
96-079a	10.1	22.1	2.24	2.32	0.16	2.37	0.03	i 0.04	7.98	8.93	0.34	9.29	0.13	i 0.36

^a Where yr is the year, doy is the day of the year, and x is the pass designator (a, b, c, etc.).

^b Determined from surface meteorological data.

^c Determined from fit to TPR data.

^d Determined from linear fit to WVR 31.4 GHz during the period of fit of BWG TPR data and corrected to X-band.

^e T_{atm} (BWG) _i T_{atm} (WVR).

^f Determined from linear fit to WVR 31.4 GHz during the period of fit of BWG TPR data.

Table 1 (cont'd).

(1) Experiment ID, yr-doyx ^a	(2) Min. elev. angle over fit TPR data, deg	(3) Max. elev. angle over fit TPR data, deg	(4) X-band T_{atm} at zenith, ^b K	(5) X-band T_{atm} at zenith, ^c K	(6) Est. $\frac{3}{4}$ of (5), K	(7) X-band T_{atm} at zenith, ^d K	(8) Est. $\frac{3}{4}$ of (7), K	(9) Difference of (5) and (7), ^e K	(10) Ka-band T_{atm} at zenith, ^b K	(11) Ka-band T_{atm} at zenith, ^c K	(12) Est. $\frac{3}{4}$ of (11), K	(13) Ka-band T_{atm} at zenith, ^f K	(14) Est. $\frac{3}{4}$ of (13), K	(15) Difference of (11) and (13) ^e
96-079b	10.3	73.5	2.32	2.37	0.12	2.36	0.02	0.01	8.89	9.44	0.41	9.17	0.09	0.27
96-088a	10.4	76.9	2.27	2.41	0.87	2.41	0.03	0.00	8.75	10.34	0.67	10.24	0.11	0.10
96-088b	10.1	19.1	2.34	2.32	0.27	2.38	0.02	i 0.06	9.51	9.22	0.29	9.61	0.08	i 0.39
96-088c	10.1	12.7	2.48	2.53	0.34	—	—	—	11.32	11.86	1.41	—	—	—
96-089a	10.2	64.4	2.47	2.64	1.00	—	—	—	11.19	13.26	7.49	—	—	—
96-089b	10.2	24.2	2.42	2.50	0.21	—	—	—	10.49	11.48	0.84	—	—	—
96-089c	10.1	14.7	2.15	2.24	0.15	—	—	—	6.66	7.77	0.31	—	—	—
96-089d	10.3	88.0	2.16	2.27	0.13	—	—	—	6.63	7.99	0.44	—	—	—
96-089e	10.2	19.5	2.15	2.28	0.55	—	—	—	6.63	8.24	0.26	—	—	—
96-092a	10.2	49.9	2.32	2.30	0.10	—	—	—	9.09	8.91	0.64	—	—	—
96-092b	10.3	33.2	2.37	—	—	—	—	—	9.75	10.61	0.40	—	—	—
96-093a	10.3	40.4	2.45	2.30	0.14	—	—	—	10.57	8.61	0.47	—	—	—
96-093b	10.4	39.7	2.44	2.38	0.14	—	—	—	10.51	9.67	0.24	—	—	—
96-094a	10.1	22.2	2.25	—	—	2.45	0.07	—	8.36	10.62	0.63	11.20	0.30	i 0.59
96-095a	10.2	80.7	2.22	2.41	0.68	2.45	0.03	i 0.04	8.02	10.26	1.09	11.16	0.15	i 0.90
96-095b	10.1	13.4	2.29	2.47	0.40	2.45	0.01	0.03	8.73	10.90	0.34	11.07	0.06	i 0.17
96-100a	10.1	42.9	2.12	2.22	0.53	2.35	0.01	i 0.13	6.90	8.11	0.50	8.95	0.04	i 0.84
96-100b	10.2	41.5	2.15	2.23	0.58	2.36	0.17	i 0.13	7.17	8.14	0.45	9.16	0.67	i 1.02
96-102a	10.1	25.5	2.14	2.34	0.57	2.39	0.03	i 0.05	7.11	9.48	1.11	9.86	0.13	i 0.38
96-103a	10.2	73.0	2.25	2.35	0.68	2.41	0.04	i 0.06	8.29	9.53	1.01	10.29	0.16	i 0.76
96-113a	10.2	16.4	2.20	2.39	0.43	2.44	0.04	i 0.05	7.71	9.99	0.69	10.93	0.17	i 0.94
96-114a	10.4	76.0	2.20	2.40	0.65	2.44	0.02	i 0.04	7.71	10.08	1.02	10.90	0.07	i 0.82
96-114b	10.3	22.2	2.20	2.37	0.18	2.43	0.01	i 0.06	7.61	9.69	0.57	10.77	0.05	i 1.08
96-116a	10.4	53.9	2.45	2.49	0.54	2.50	0.06	i 0.01	11.07	11.50	0.98	12.22	0.31	i 0.72

^a Where yr is the year, doy is the day of the year, and x is the pass designator (a, b, c, etc.).

^b Determined from surface meteorological data.

^c Determined from fit to TPR data.

^d Determined from linear fit to WVR 31.4 GHz during the period of fit of BWG TPR data and corrected to X-band.

^e T_{atm} (BWG) i T_{atm} (WVR).

^f Determined from linear fit to WVR 31.4 GHz during the period of fit of BWG TPR data.

Table 1 (cont'd).

(1) Experiment ID, yr-doyx ^a	(2) Min. elev. angle over fit TPR data, deg	(3) Max. elev. angle over fit TPR data, deg	(4) X-band T_{atm} at zenith, ^b K	(5) X-band T_{atm} at zenith, ^c K	(6) Est. $\frac{3}{4}$ of (5), K	(7) X-band T_{atm} at zenith, ^d K	(8) Est. $\frac{3}{4}$ of (7), K	(9) Difference of (5) and (7), ^e K	(10) Ka-band T_{atm} at zenith, ^b K	(11) Ka-band T_{atm} at zenith, ^c K	(12) Est. $\frac{3}{4}$ of (11), K	(13) Ka-band T_{atm} at zenith, ^f K	(14) Est. $\frac{3}{4}$ of (13), K	(15) Difference of (11) and (13) ^e
96-116b	10.2	33.4	2.44	2.47	0.36	2.49	0.08	i 0.02	10.91	11.19	0.77	11.99	0.38	i 0.80
96-117a	10.3	45.2	2.26	2.31	0.53	2.41	0.03	i 0.10	8.71	9.25	0.34	10.28	0.13	i 1.03
96-117b	10.2	40.4	2.26	2.27	0.59	2.40	0.01	i 0.13	8.58	8.64	0.98	10.08	0.06	i 1.44
96-117c	10.3	53.0	2.27	2.41	0.14	2.49	0.07	i 0.07	8.49	10.24	0.63	11.94	0.32	i 1.70
96-117d	10.3	23.7	2.26	2.47	0.32	2.45	0.01	0.02	8.48	11.00	0.25	11.21	0.04	i 0.21
96-120a	10.2	22.0	2.08	—	—	2.34	0.07	—	6.16	8.02	0.56	8.69	0.26	i 0.67
96-121a	10.4	82.9	2.07	2.24	0.72	2.36	0.06	i 0.12	6.09	8.12	0.96	9.03	0.23	i 0.91
96-121b	10.1	15.0	2.08	2.23	0.30	2.34	0.02	i 0.12	6.08	7.84	0.11	8.74	0.09	i 0.91
96-122a	10.1	14.6	2.17	2.26	0.38	2.41	0.00	i 0.15	7.73	8.77	0.88	10.30	0.02	i 1.53
96-123a	10.1	71.1	2.16	2.26	0.64	2.40	0.05	i 0.14	7.56	8.75	1.23	9.97	0.20	i 1.21
96-123b	10.1	23.8	2.23	2.23	0.27	2.42	0.00	i 0.19	8.35	8.33	0.46	10.56	0.01	i 2.23
96-125a	10.3	49.9	2.15	2.17	0.48	2.35	0.03	i 0.19	7.42	7.61	0.79	8.94	0.10	i 1.33
96-125b	10.2	35.5	2.15	2.20	0.44	2.33	0.01	i 0.13	7.36	7.91	0.65	8.42	0.05	i 0.51
96-127b	10.4	29.9	2.33	2.39	0.27	2.41	0.07	i 0.01	9.32	10.01	0.24	10.20	0.31	i 0.19
96-128a	10.1	23.8	2.24	—	—	2.42	0.07	—	8.52	9.96	0.63	10.45	0.32	i 0.49
96-129a	10.3	74.6	2.23	2.30	0.67	2.40	0.01	i 0.10	8.38	9.17	0.72	10.03	0.05	i 0.86
96-129b	10.1	19.5	2.23	2.27	0.43	2.41	0.06	i 0.14	8.39	8.91	0.44	10.35	0.25	i 1.44
96-130a	10.3	87.9	2.23	2.26	0.78	2.38	0.03	i 0.12	8.40	8.73	1.01	9.56	0.14	i 0.83
96-145b	10.2	34.6	2.51	—	—	—	—	—	11.31	15.91	3.61	—	—	—
96-150a	10.3	53.8	2.24	2.28	0.31	2.41	0.04	i 0.13	8.45	8.95	1.01	10.31	0.16	i 1.36
96-150b	10.2	26.4	2.22	2.34	0.28	2.42	0.03	i 0.08	8.22	9.69	0.18	10.49	0.11	i 0.80
96-151a	10.1	43.6	2.26	2.34	0.47	2.41	0.06	i 0.06	8.73	9.77	0.85	10.24	0.26	i 0.47
96-151b	10.3	32.5	2.36	2.31	0.17	2.39	0.03	i 0.08	9.92	9.29	0.44	9.90	0.13	i 0.61
96-151c	10.3	52.9	2.41	2.36	0.39	2.37	0.05	i 0.01	10.27	9.58	0.67	9.45	0.21	0.13

^a Where yr is the year, doy is the day of the year, and x is the pass designator (a, b, c, etc.).

^b Determined from surface meteorological data.

^c Determined from fit to TPR data.

^d Determined from linear fit to WVR 31.4 GHz during the period of fit of BWG TPR data and corrected to X-band.

^e T_{atm} (BWG) i T_{atm} (WVR).

^f Determined from linear fit to WVR 31.4 GHz during the period of fit of BWG TPR data.

Table 1 (cont'd).

(1) Experiment ID, yr-doyx ^a	(2) Min. elev. angle over fit TPR data, deg	(3) Max. elev. angle over fit TPR data, deg	(4) X-band T_{atm} at zenith, ^b K	(5) X-band T_{atm} at zenith, ^c K	(6) Est. $\frac{3}{4}$ of (5), K	(7) X-band T_{atm} at zenith, ^d K	(8) Est. $\frac{3}{4}$ of (7), K	(9) Difference of (5) and (7), ^e K	(10) Ka-band T_{atm} at zenith, ^b K	(11) Ka-band T_{atm} at zenith, ^c K	(12) Est. $\frac{3}{4}$ of (11), K	(13) Ka-band T_{atm} at zenith, ^f K	(14) Est. $\frac{3}{4}$ of (13), K	(15) Difference of (11) and (13) ^e
96-151d	10.3	18.9	2.41	2.48	0.66	2.37	0.01	0.10	10.28	11.04	0.18	9.47	0.06	1.57
96-200a	10.3	66.9	2.36	2.41	0.77	2.47	0.01	i 0.06	10.12	10.69	1.37	11.60	0.05	i 0.90
96-200b	10.1	13.1	2.47	2.37	0.49	2.43	0.00	i 0.06	11.36	10.08	0.52	10.72	0.01	i 0.64
96-200c	10.2	16.9	2.39	2.23	0.27	2.32	0.08	i 0.09	10.16	8.16	0.65	8.18	0.30	i 0.02
96-200d	10.1	85.4	2.39	2.24	0.18	2.33	0.04	i 0.09	10.09	8.31	0.82	8.45	0.13	i 0.15
96-201a	10.2	13.1	2.41	2.30	0.12	2.37	0.16	i 0.07	10.28	8.95	0.22	9.44	0.64	i 0.49
96-201b	10.2	80.4	2.37	2.35	0.11	2.38	0.04	i 0.03	9.87	9.60	0.50	9.53	0.17	0.07
96-219a	10.1	11.6	2.60	2.39	0.13	2.43	0.05	i 0.04	12.62	10.03	0.26	10.70	0.21	i 0.67
96-219b	10.3	71.2	2.63	2.53	0.19	2.50	0.05	0.02	12.92	11.64	0.46	12.31	0.26	i 0.67
96-219c	10.3	26.2	2.66	2.58	0.30	2.52	0.11	0.06	13.36	12.33	0.51	12.57	0.56	i 0.24
96-220a	10.2	36.4	2.43	2.45	0.87	2.49	0.03	i 0.03	10.95	11.17	1.50	11.99	0.12	i 0.82
96-220b	10.4	32.0	2.37	2.40	0.70	2.48	0.01	i 0.08	10.14	10.47	0.80	11.74	0.05	i 1.26
96-220d	10.2	59.6	2.55	2.54	0.13	2.52	0.06	0.02	12.05	11.95	0.42	12.71	0.31	i 0.76
96-220e	10.2	31.4	2.48	2.57	0.23	2.50	0.00	0.07	11.26	12.32	0.58	12.25	0.02	0.07
96-222a	10.1	41.1	2.52	2.62	0.17	2.58	0.04	0.04	11.72	12.89	0.65	13.85	0.22	i 0.96
96-222b	10.3	44.6	2.42	2.65	0.17	2.57	0.03	0.08	10.61	13.32	0.72	13.57	0.15	i 0.25
96-228c	10.2	28.3	2.89	2.89	0.23	2.69	0.04	0.19	16.22	16.11	1.22	15.90	0.25	0.22
96-229a	10.3	35.3	2.49	2.72	0.68	2.69	0.02	0.03	11.64	14.41	1.35	15.82	0.13	i 1.42
96-229b	10.2	37.6	2.47	2.71	0.71	2.68	0.02	0.03	11.39	14.28	1.68	15.67	0.11	i 1.39
96-229c	10.1	55.6	2.68	2.76	0.45	2.69	0.02	0.07	13.74	14.65	0.68	15.85	0.11	i 1.20
96-229d	10.2	33.7	2.72	2.81	0.19	2.73	0.03	0.08	14.27	15.21	0.57	16.54	0.16	i 1.33
96-241a	10.2	28.0	2.20	2.38	0.16	2.44	0.05	i 0.05	7.85	10.03	0.39	10.87	0.20	i 0.83
96-241b	10.2	60.1	2.19	2.43	0.18	2.46	0.05	i 0.03	7.72	10.68	0.47	11.47	0.24	i 0.78
96-242a	10.1	13.5	2.35	2.55	0.46	2.54	0.00	0.01	10.04	12.40	0.38	13.07	0.02	i 0.66

^a Where yr is the year, doy is the day of the year, and x is the pass designator (a, b, c, etc.).

^b Determined from surface meteorological data.

^c Determined from fit to TPR data.

^d Determined from linear fit to WVR 31.4 GHz during the period of fit of BWG TPR data and corrected to X-band.

^e T_{atm} (BWG) _i T_{atm} (WVR).

^f Determined from linear fit to WVR 31.4 GHz during the period of fit of BWG TPR data.

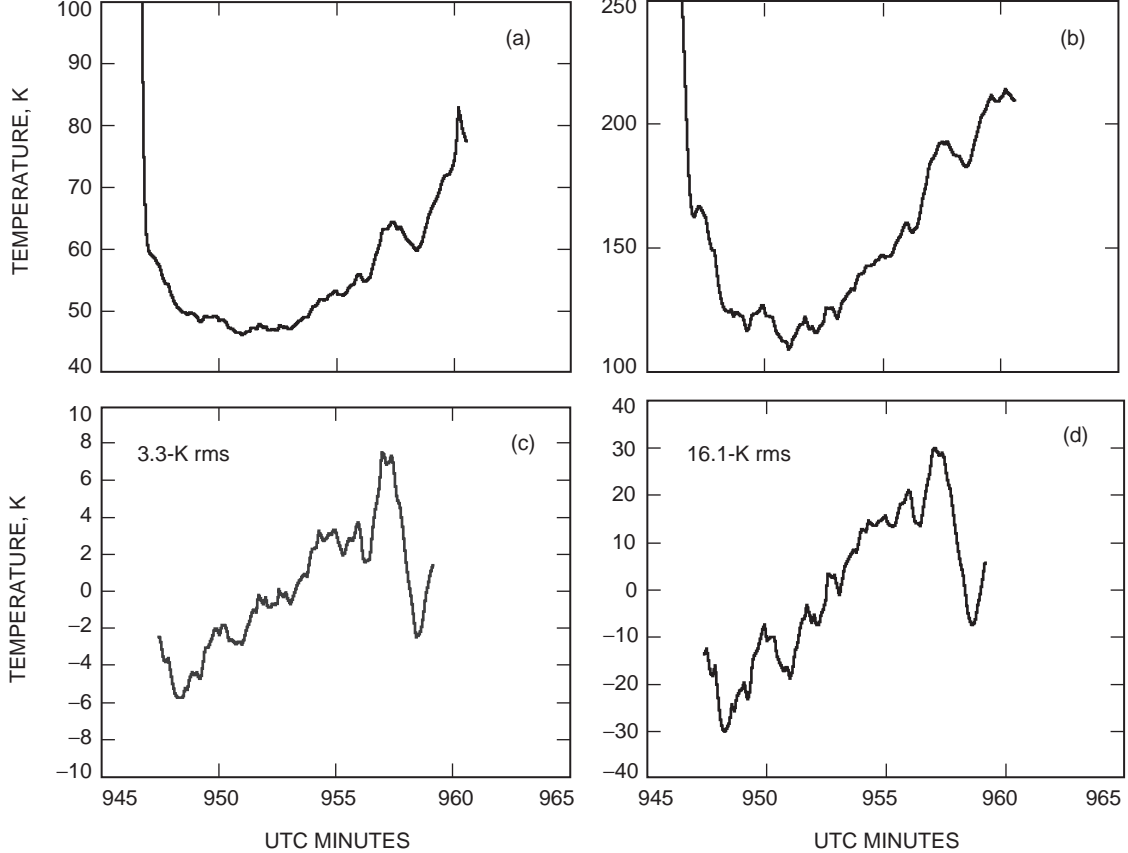


Fig. 4. Examples of cloudy-/rainy-weather data acquired during pass 96-073d: (a) raw X-band T_{op} data, (b) raw Ka-band T_{op} data, (c) X-band postfit residuals using the model derived from the Ka-band postfit solution, and (d) Ka-band postfit residuals corresponding to the fit of the data of Fig. 4(b).

passes and up to many times the gain instability (as high as 16 K) during turbulent-weather passes. The thermal noise contributions over the TPR filter bandpasses are negligible (less than 0.01 K).

The uncertainty in the model is believed to lie below 0.5 K in the elevation-angle-dependent signature of the nonatmospheric antenna model, $T_{ant}(\theta)$, and is attributed primarily to tripod scatter and back-lobe pickup. The a priori antenna model used in Eq. (1) was derived empirically at X-band using clear-weather data acquired during a previous study at higher elevation angles (above 20 deg), where spillover effects were considered negligible [2]. This antenna temperature-versus-elevation angle model was used at Ka-band for this study, based on the assumption that both the X-band and Ka-band wavelengths are much smaller than the physical dimensions of the tripod struts.

The integrity of the model was tested by performing fits on individual one-air-mass segments at different elevation-angle arcs and comparing the results with those of the fit over all of the data for specific passes. The agreement was consistent with the 0.5-K uncertainty.

The X-band data were not fitted for this study because the usable elevation angle ranges were much lower than those in the previous study [2]. At the lower elevation angles, the forward spillover is believed to be larger at X-band than at Ka-band. The spillover (both forward and rear) are subjects for the proposed future study of the X-band data.

Once an opacity for water vapor is determined from the data, the one-air-mass atmospheric noise temperature is estimated using Eq. (3), with $\theta = 90$ deg. Table 2 summarizes the statistical results of the

Table 2. One-air-mass atmospheric-noise temperature statistics.

System	Band	Mean, K	rms, K	Minimum, K	Maximum, K	Number of observations
BWG	X	2.45	0.35	2.17	6.53	181
WVR	X	2.45	0.10	2.32	2.73	115
MODEL	X	2.34	0.15	2.07	2.89	173
BWG	Ka	10.64	3.95	7.26	56.19	192
WVR	Ka	11.01	1.98	8.08	16.54	115
MODEL	Ka	9.38	1.83	6.08	16.22	173

estimated one-air-mass (or equivalent-zenith) atmospheric noise temperatures found from the data for each of the 192 passes. Also presented in Table 2 are the values derived from the concurrent WVR data and concurrent surface-model atmospheric-noise-temperature estimates, using meteorological measurements acquired during the pass as input. Note that not all 192 Ka-band passes included concurrent WVR data, surface-weather data, or X-band data. Of the 192 passes where Ka-band BWG T_{atm} was measured, 115 of these included usable concurrent WVR data and 173 included concurrent available surface meteorological data.

Note in Table 2 that the maximum T_{atm} estimates for the WVR and weather-model data sets lie significantly below those of the BWG. The WVR does not produce usable data during rainy conditions, and the surface model cannot account for the nonuniform distribution of water content in clouds, which are not accounted for in the meteorological measurements at the surface. The BWG data set thus includes estimates for passes when rain was known to have occurred, and, therefore, it extends over a wider range of T_{atm} , which also is reflected in the higher rms scatters of the data sets.

The average Ka-band one-air-mass T_{atm} over 192 passes agrees with that of the WVR averaged from 115 passes to within 0.4 K, as noted in Table 2. However, if we consider only the 115 data sets in common between the BWG and WVR, the average value of the differences ($T_{BWG} - T_{WVR}$) is -0.52 K, with an rms scatter of 0.74 K over the 115 common data points. This result is consistent with the assumed 0.5-K absolute calibration errors of each system.

The histogram of Fig. 5 illustrates the number of passes for 0.5-K bins of the Ka-band ($T_{BWG} - T_{WVR}$) difference for the 115 common passes as well as a Gaussian fit to the data points. The Gaussian fit peaks at about -0.6 K, consistent with the resultant -0.52 -K average of the differences, well within the resolution of the 0.5-K bin sizes.

For visual inspection of the actual values of BWG and WVR data, refer to Fig. 6, which displays the BWG T_{atm} plotted against the WVR T_{atm} value for each of the 115 common passes. The two sets of measurements generally follow the expected line of unity slope and origin intercept with a sizable scatter about the line. Indeed, a linear fit of the 115 data points yields the following result:

$$T_{BWG} = (0.96 \pm 0.04)T_{WVR} - (0.12 \pm 0.40)$$

with a 0.74-K rms scatter about the fitted line. Thus, the one-air-mass T_{atm} for the BWG and the WVR are in general agreement, consistent with the 0.5-K absolute uncertainty of both systems (77 percent of the data points have T_{atm} within 1 K of each other). The larger differences could be explained by the two systems sampling spatially different areas of the sky.

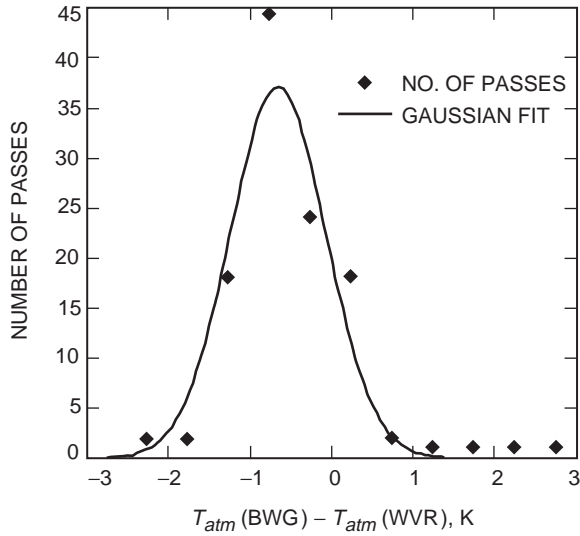


Fig. 5. The number of passes for 0.5-K bins of the ($T_{\text{BWG}} - T_{\text{WVR}}$) difference for the 115 common BWG and WVR passes as well as a Gaussian fit to the points.

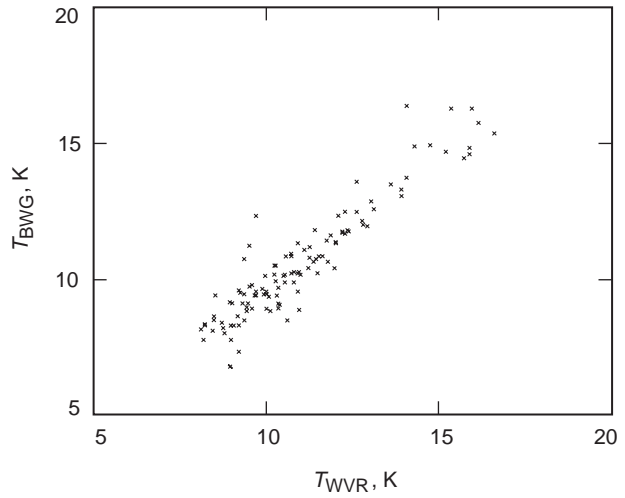


Fig. 6. The BWG T_{atm} versus the WVR T_{atm} for each of the 115 common passes.

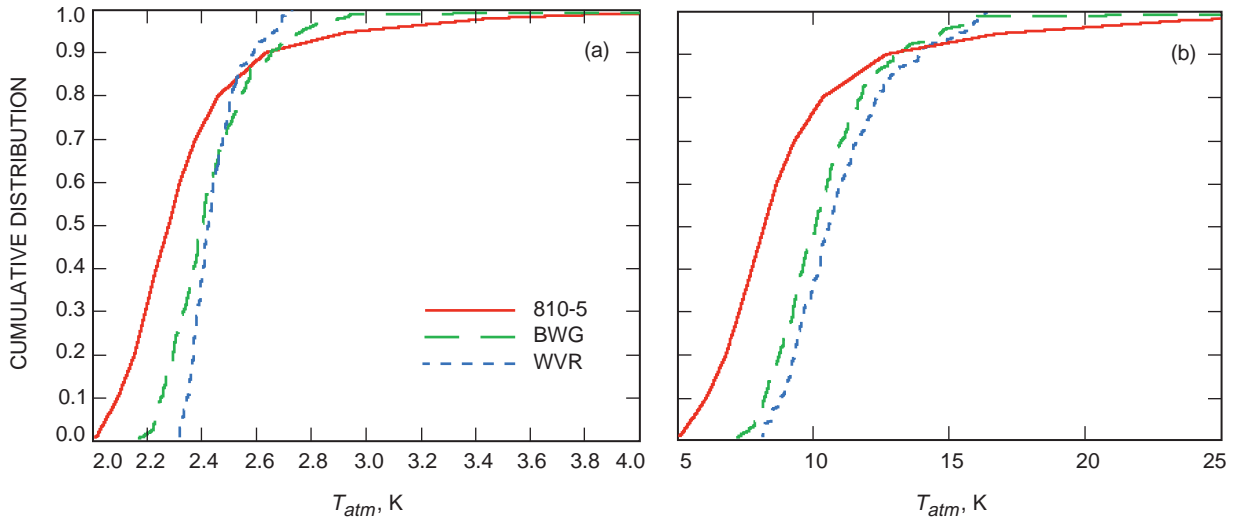


Fig. 7. Cumulative distributions of one-air-mass (equivalent-zenith) T_{atm} measurements: (a) X-band and (b) Ka-band. Each figure shows the curves for the measured BWG and WVR values and that from 810-5.

Figures 7(a) and 7(b) display the X-band and Ka-band cumulative distributions, respectively, for the BWG and WVR one-air-mass (equivalent-zenith) T_{atm} measurements along with those from the *Deep Space Network/Flight Project Interface Design Handbook* (810-5).⁵ These curves are used by planners of flight projects to evaluate station-to-spacecraft link budgets. In such link budgets, the atmospheric attenuation and noise temperature at 90 or 95 percent weather usually are used. Notice that, for values of Ka-band T_{atm} below the 90 percent cumulative distribution in Fig. 7(b), the 810-5 curve is optimistic, and above 90 percent, the 810-5 curve is pessimistic relative to the corresponding BWG and WVR curves. The WVR and BWG curves track each other within 0.5 K, with the BWG T_{atm} lying below that of the

⁵ *Deep Space Network/Flight Project Interface Design Handbook*, vol. I, *Existing Capabilities*, JPL 810-5 (internal document), Module TCI-40, Jet Propulsion Laboratory, Pasadena, California, pp. 5–6, May 1, 1992.

WVR for a given cumulative distribution value. The WVR cumulative distribution does not include rainy weather data. However, the BWG cumulative distribution curve extends to much higher T_{atm} , as it does include rainy weather passes. The closer agreement of the BWG and WVR cumulative distribution curves suggests that the high-end cumulative distributions at 90 to 95 percent weather at Goldstone, used for spacecraft link budgets, can be relaxed over those inferred from the 810-5 curves.

V. Conclusion

The study reported on demonstrates that the BWG Ka-band one-air-mass T_{atm} estimates provide valid atmospheric noise temperatures (and hence attenuation). This assertion is reinforced by demonstrated agreement with independent values derived from the WVR 31.4-GHz channel. The BWG also can measure estimates of one-air-mass T_{atm} during turbulent or rainy-weather conditions. Differences with the WVR typically are within the absolute calibration uncertainty of both systems, and higher differences can be explained by each system sampling different areas of the sky.

Proposed future work includes (1) using the Ka-band estimates to solve for the X-band antenna spillover model at low elevation angles and then fitting the X-band data to solve for their own estimates of T_{atm} at one air mass, (2) partitioning clear- and turbulent-weather passes into segments and analyzing the resulting statistics within a pass, and (3) correlating the fluctuation in the T_{op} postfit residuals with received Doppler fluctuations from Mars Global Surveyor (MGS)/Ka-Band Link Experiment (KaBLE-II) and SURFSAT-1 signal data.

Acknowledgments

We would like to thank the DSS-13 station personnel for conducting the experiments and acquiring the data: G. Bury, C. Goodson, L. Smith, G. Farner, R. Reese, R. Littlefair, J. Crook, J. Garnica, L. Skjerve, and L. Tanida. We also would like to thank S. Keihm for processing and delivering the WVR data and for contributing descriptions of the R6 and J3 WVRs.

References

- [1] C. T. Stelzried and M. J. Klein, "Precision DSN Radiometer Systems: Impact on Microwave Calibrations," *Proc. of the IEEE*, vol. 82, pp. 776–787, May 1994.
- [2] S. J. Keihm, "Water Vapor Radiometer Measurements of the Tropospheric Delay Fluctuations at Goldstone Over a Full Year," *The Telecommunications and Data Acquisition Progress Report 42-122, April–June 1995*, Jet Propulsion Laboratory, Pasadena, California, pp. 1–11, August 15, 1995.
http://tda.jpl.nasa.gov/tda/progress_report/42-122/122J.pdf
- [3] F. T. Ulaby, R. K. Moore, and A. K. Fung, *Microwave Remote Sensing Active and Passive*, vol. I, *Microwave Remote Sensing Fundamentals and Radiometry*, Reading, Massachusetts: Addison-Wesley Publishing Company, 1981.

- [4] D. D. Morabito and L. Skjerve, “Analysis of Tipping-Curve Measurements Performed at the DSS-13 Beam-Waveguide Antenna at 32.0 and 8.45 Gigahertz,” *The Telecommunications and Data Acquisition Progress Report 42-122, April–June 1995*, Jet Propulsion Laboratory, Pasadena, California, pp. 151–174, August 15, 1995.
<http://tda.jpl.nasa.gov/tda/progress-report/42-122/122C.pdf>
- [5] M. L. Kutner, “Application of a Two-Layer Atmospheric Model to the Calibration of Millimeter Observations,” *Astrophysical Letters*, vol. 19, pp. 81–87, 1978.